International Forum on Aeroelasticity and Structural Dynamics
IFASD 2017
25-28 June 2017 Como, Italy

UNCERTAINTY QUANTIFICATION IN THE VICINITY OF MODE SWITCHES IN THE FLUTTER RESPONSE OF A COMPOSITE CANTILEVERED WING

Christian T. Nitschke[1], **Angela Vincenti**[1], **Jean-Camille Chassaing**[1]

[1]Sorbonne Universités, UPMC Paris 06, CNRS, UMR 7190, Institut Jean le Rond d'Alembert
4 place Jussieu, 75005 Paris, France
christian.nitschke@upmc.fr
angela.vincenti@upmc.fr
jean-camille.chassaing@upmc.fr

Keywords: aeroelasticity, uncertainty quantification, composite materials, polynomial chaos, machine learning

Abstract: In composite wings, abrupt switches in modal behaviour occur depending on the elastic properties of the laminate. These switches can lead to drastic drops in critical flutter velocity. The modal behaviour is so sensitive that even small fabrication errors can cause them. In this paper, several laminate configurations prone to mode switches are studied and the effect of errors on angular ply placement and thickness on the aeroelastic behaviour are examined. The polar method is used for the analysis of the stiffness properties of the materials and their distribution. Arbitrary polynomial chaos is used to accelerate the stochastic propagation step. The discontinuties in the response surface are treated by using machine learning.

1 INTRODUCTION

As composite materials provide highly favorable stiffness-to-weight ratios, this type of material has gained broader adoption in aircraft manufacturing in recent years. However, in comparison to classical aircraft materials, as for example aluminium, their stiffness is anisotropic. As studies conducted in the early 1980s in structural dynamics [1] and aeroelasticity [2] have demonstrated, the consequences of the anisotropy are important for the modal response of structures.

As these materials consist of different plies which are assembled during a manufacturing process, errors can occur in this assembly, which in turn alter the elastic properties of the material. This can lead to said deviations in modal behaviour. In the case of aeroelastic problems, it also can lead to substantial differences in the critical flutter velocity. Typical uncertainties in this framework are errors in the ply angles as well as in the ply thicknesses [3, 4], which are the constitutive parameters of the laminate's stacking sequence.

Applying uncertainty quantification directly on these uncertainties means that the number of parameters is dependent on the number of plies. In aeronautic construction, laminates with 16 or more plies are not unusual, which means that the number of uncertain constitutive parameters gets quickly very high (32 or more) and the interpretation of the problem is confusing. The high number of uncertain parameters also prevents deployment of advanced uncertainty quantification methods such as polynomial chaos or stochastic collocation [5]

In order to solve that problem, Scarth et al. [6] used the so-called lamination parameters, which provide a smaller set of parameters to describe the behaviour of a laminate in place of the whole set of uncertain constitutive parameters. However, many of the lamination parameters do not have an immediate physical meaning. Moreover, this approach is inflexible in the consideration of ply thicknesses. This is why the polar method is considered in this paper, which was first introduced by [7] and reformalised later by [8]. The polar method permits to take into account uncertainty in the ply thicknesses and allows for more general laminate configurations while keeping the number of uncertain parameters down at six even in non-symmetric cases.

Uncertainty quantification by Monte Carlo simulation has the disadvantage of a very high computational cost. Polynomial chaos methods [9] have therefore gained popularity, particularly in the aerodynamics and aeroelasticity community [10, 11, 12]. However, classical generalised polynomial chaos is based on a scheme of associations of a small number of known distributions, the so-called Wiener-Askey scheme. Moreover, it supposes that the parameters are independent. Either of the aforementioned approaches (lamination parameters or the polar method) introduces non-standard, correlated variables. This problem is solved in Scarth et al. [6] by decorrelating the lamination parameters using a Rosenblatt decomposition. However, this requires either knowledge or approximation of the conditional cumulative density functions, which are tedious to compute. Soize and Ghanem [13] extended the generalised polynomial chaos approach to arbitrary distributions, which was later demonstrated by [14] to work with correlated variables. This method was used in [15] to directly take into account the polar parameters.

One of the major challenges in polynomial chaos is taking into account discontinuous response surfaces, as they occur in the composite wing flutter problem due to switching of modal behaviour [6]. In the present work, we address this problem proposing a fully automatic procedure for response surface splitting, which is based on machine learning and trained on a preliminary set of samples.

In Section 2, a brief introductory summary to the polar method will be given, before presenting the aeroelastic problem in Section 3. In Section 4, we detail the uncertainty quantification framework, including the steps involving machine learning which are needed to take into account mode switches and the resulting discontinuities in the response surface. In Section 5, we first give a deterministic analysis of the critical flutter velocity for composite cantilever wings, resulting in a response surface that highlights the occurrence of mode switches as a function of the material. Then, based on the deterministic results, a number of laminate configurations are selected. The chosen configurations correspond to points on the response surface which are near the discontinuity. Uncertainty quantification on ply thicknesses and angles is subsequently conducted on these configurations according to the method proposed in Section 4.

2 THE POLAR METHOD

Any two-dimensional symmetric positive-definite tensor can be represented by polar constants which are given by [8]

$$
\begin{aligned}
8T_0 &= Q_{xx} - 2Q_{xy} + 4Q_{ss} + Q_{yy} && (1)\\
8T_1 &= Q_{xx} + 2Q_{xy} + Q_{yy} && (2)\\
8R_0 e^{\imath 4\Phi_0} &= Q_{xx} + 4\imath Q_{xs} - 2Q_{xy} - 4Q_{ss} - 4\imath Q_{ys} + Q_{yy} && (3)\\
8R_1 e^{\imath 2\Phi_1} &= Q_{xx} + 2\imath Q_{xs} + 2\imath Q_{ys} - Q_{yy} && (4)
\end{aligned}
$$

With the method applied to elastic material behaviour, the modules T_0 and T_1 represent the isotropic part. R_0 and R_1 are the modules of the anisotropic behavior, Φ_0 and Φ_1 being the corresponding orientation angles, which depend on the reference frame. T_0, T_1, R_0, R_1 and the difference between the orientation angles $\Phi_0 - \Phi_1$ do not change under rotation of the reference frame, which is why they are called polar invariants.

The polar constants can be transformed back into cartesian components using the following equations [8]

$$
\begin{aligned}
Q_{xx} &= T_0 + 2T_1 + R_0\cos(4\Phi_0) + 4R_1\cos(2\Phi_1) && (5)\\
Q_{xy} &= -T_0 + 2T_1 - R_0\cos(4\Phi_0) && (6)\\
Q_{xs} &= R_0\sin(4\Phi_0) + 2R_1\sin(2\Phi_1) && (7)\\
Q_{yy} &= T_0 + 2T_1 + R_0\cos(4\Phi_0) - 4R_1\cos(2\Phi_1) && (8)\\
Q_{ys} &= -R_0\sin(4\Phi_0) + 2R_1\sin(2\Phi_1) && (9)\\
Q_{ss} &= T_0 - R_0\cos(4\Phi_0) && (10)
\end{aligned}
$$

Another advantage of the method consists in its representation of material symmetries, which is linked to very simple criteria summed up in Table 1.

Elastic symmetry	Polar condition
Orthotropy	$\Phi_0 - \Phi_1 = K\frac{\pi}{4}, K \in \{0, 1\}$
R_0-Orthotropy	$R_0 = 0$
Square Symmetry	$R_1 = 0$
Isotropy	$R_0 = R_1 = 0$

Table 1: Conditions for elastic symmetries in terms of polar invariants [8]

In the isotropic case, obviously, the anisotropic moduli are zero. Orthotropic materials have a difference between their orientation angles of multiples of $\frac{\pi}{4}$. Furthermore, there are two special cases of orthotropy, each linked to elimination of one of the anisotropic constants. The classical case of square symmetry is linked to R_1 being zero. For R_0 being zero, [16] distinguishes another special material symmetry, which he calls R_0-orthotropy after its symmetry criterion.

Naturally, the values which the polar parameters can take are limited by thermodynamic constraints, to which geometric constraints coming from angle sequences and their distribution along the thickness of the plate must be added in case of laminate layups [17].

In case of an orthotropic laminate with plies made of the same base material, these bounds are

given by the equations [17]

$$0 \leq R_0 \tag{11}$$

$$0 \leq R_1 \tag{12}$$

$$R_0 \leq R_0^{max} \tag{13}$$

$$2\left(\frac{R_1}{R_1^{max}}\right)^2 - 1 \leq (-1)^{K-K^{BM}}\left(\frac{R_0}{R_0^{max}}\right) \tag{14}$$

Eqs. (11) - (14) thus represent the borders of the domain of existence of orthotropic laminates. This domain is depicted in Fig. 1.

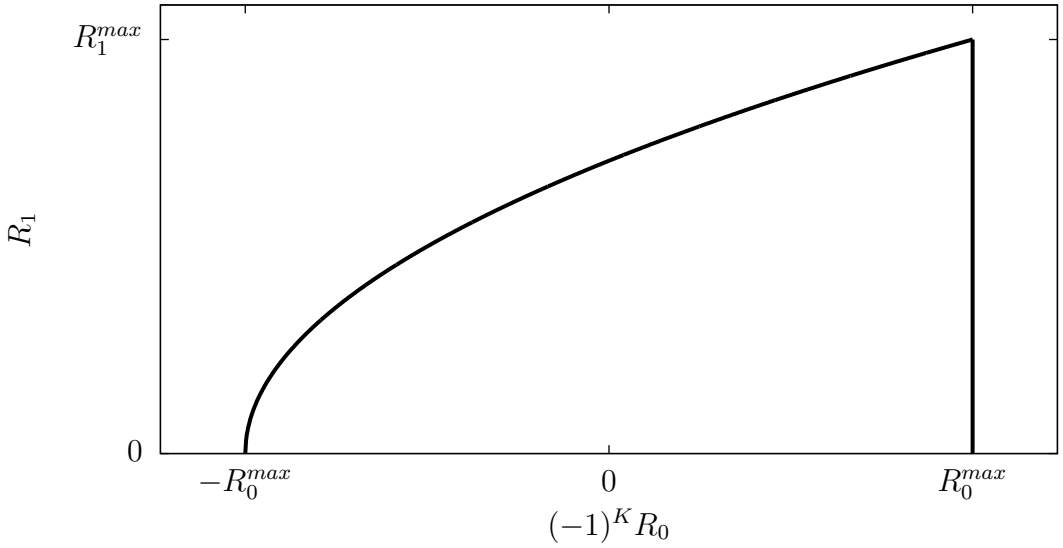

Figure 1: Limits of the polar domain for orthotropic laminates

3 AEROELASTIC PROBLEM

The aeroelastic model employed in this work is built after [6, 18, 19], which is a straight cantilevered composite plate-wing model with strip-theory flutter derivatives aerodynamics where the number of flutter derivatives has been reduced to one. A scheme of the implied physical wing is given in Fig. 2.

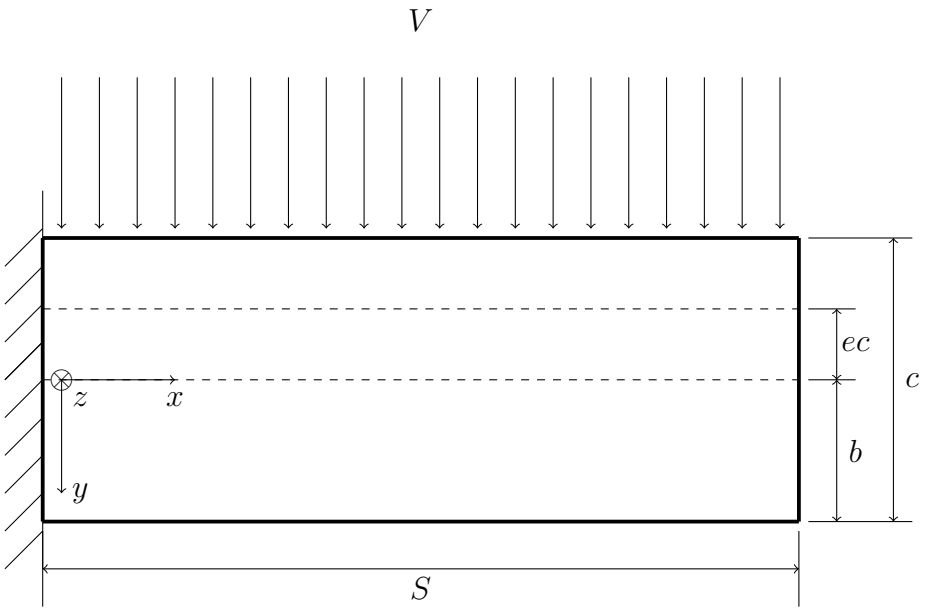

Figure 2: Scheme of the cantilevered plate wing

The reference axis is the mid-chord span-wise axis, which coincides with the x axis in the model. The fibre zero-angle direction is also aligned to this axis. The aerodynamic centre at which the lift line forces are applied is at $y = -ec$, e being an excentricity factor which is rendered dimensionless by the chord length. The chord is noted c, the half chord b, and the half span S. The freestream velocity V is in the direction of the y axis. The vertical axis z is positive downwards.

In order to produce comparable results, all simulations in this work will be carried out using the said model with the geometric and aeromechanical parameters given by [19], which we recall in Table 2

Wing half span $S[m]$	Chord $c[m]$	Air density $\rho_a \left[kg/m^3\right]$	Lift excentricity e	Unsteady parameter $M_{\dot{\theta}}$
0.3048	0.0762	1.225	0.25	-1.2

Table 2: Wing geometry and aeromechanical data [6]

For the structural calculations, we use Classical Laminated Plate Theory (CLPT). The membrane forces $\mathbf{n}$ and the bending moments $\mathbf{m}$ are calculated form the in-plane strain $\boldsymbol{\epsilon}$ and the curvature $\boldsymbol{\kappa}$ as [20]

$$\begin{bmatrix} \mathbf{n} \\ \mathbf{m} \end{bmatrix} = \begin{bmatrix} \mathbf{A} & \mathbf{B} \\ \mathbf{B} & \mathbf{D} \end{bmatrix} \begin{bmatrix} \boldsymbol{\varepsilon} \\ \boldsymbol{\kappa} \end{bmatrix} \tag{15}$$

where $\mathbf{A}$ is the membrane stiffness, $\mathbf{D}$ the bending stiffness and $\mathbf{B}$ is a matrix describing the

coupling between bending and membrane effects. $\boldsymbol{\epsilon}$ and $\boldsymbol{\kappa}$ are expressed in Voigt notation as

$$\boldsymbol{\kappa} = \begin{pmatrix} -\frac{\partial^2 w}{\partial x^2} \\ -\frac{\partial^2 w}{\partial y^2} \\ -2\frac{\partial^2 w}{\partial x \partial y} \end{pmatrix} \tag{16}$$

$$\boldsymbol{\varepsilon} = \begin{pmatrix} \frac{\partial u}{\partial x} \\ \frac{\partial v}{\partial y} \\ \frac{\partial u}{\partial y} + \frac{\partial w}{\partial x} \end{pmatrix} \tag{17}$$

When there is no in-plane loading ($\mathbf{n} = 0$) and the plate is only charged with bending loads, Eq. 15 can be rearranged as

$$\mathbf{m} = \left(\mathbf{D} - \mathbf{B}\mathbf{A}^{-1}\mathbf{B}\right)\boldsymbol{\kappa} \tag{18}$$

where

$$\tilde{\mathbf{D}} = \mathbf{D} - \mathbf{B}\mathbf{A}^{-1}\mathbf{B} \tag{19}$$

is again a bending stiffness matrix, but modified to take into account the membrane-bending coupling [21].

To derive the equations of motion, the Lagrange equation is used

$$\frac{d}{dt}\left(\frac{\partial T}{\partial \dot{\mathbf{q}}}\right) + \frac{\partial U}{\partial \mathbf{q}} = \frac{\partial(\delta W)}{\partial(\delta \mathbf{q})} \tag{20}$$

where T is the kinetic energy, U the potential energy due to elasticity, δW is the virtual work of the aerodynamic and damping forces and $\mathbf{q}$ is the vector of generalised coordinates .

The energy expressions to be injected into this equation are given in the following. The elastic potential energy is given by the expression [22]

$$U = \frac{1}{2}\int\int \mathbf{m}^{\mathsf{T}}\boldsymbol{\kappa} dxdy \tag{21}$$

which can with the help of Eq. (18) be expanded to

$$U = \frac{1}{2}\int\int \boldsymbol{\kappa}^{\mathsf{T}}\tilde{\mathbf{D}}\boldsymbol{\kappa} dxdy \tag{22}$$

The kinetic energy is given by [19]

$$T = \frac{1}{2}\rho d\int\int \dot{w}^2 dxdy \tag{23}$$

where d is the total thickness of the plate, ρ is the density of the layup the plate consists of, and $\dot{w}$ is the vertical displacement velocity, the dot above w representing a derivative with respect to time.

The virtual work is expressed using the line lift l_a and the aerodynamic line moment m_a as [18]

$$\delta W = \int l_a(-\delta w)dx + \int m_a \delta\theta dx \tag{24}$$

where δw and $\delta\theta$ are virtual displacements. The lift and moment expressions are taken from [19]

$$l_a = \frac{1}{2}\rho_a V^2 c a_w \left(\theta + \frac{\dot{w}}{V}\right) \tag{25}$$

$$m_a = \frac{1}{2}\rho_a V^2 c^2 \left(e a_w \left(\theta + \frac{\dot{w}}{V}\right) + M_{\dot{\theta}} \frac{\dot{\theta} c}{4V}\right) \tag{26}$$

ρ_a is the air density, and $a_w = 2\pi\left(1 - \left(\frac{x}{S}\right)^3\right)$ is the lift curve slope along the span [19]. Coefficient $M_{\dot{\theta}} = -1.2$ [19] is an unsteady aerodynamic moment derivative, which is assumed constant.

In order to apply the Rayleigh-Ritz framework, we make an approach for the modal displacement using simple algebraic polynomials [23]

$$w(x,y) = \sum_{i=1}^{n_x}\sum_{j=1}^{n_y} q_{(ij)} \left(\frac{x}{S}\right)^{i+1} \left(\frac{y}{c}\right)^{j-1} \tag{27}$$

where

$$q_{(ij)} = \hat{q}_{(ij)} \exp(\lambda t) \tag{28}$$

θ is derived from this using a small displacement approximation $\theta \approx \sin(\theta) \approx \frac{\partial w}{\partial y}$

Injecting the mode shape approach into the energy expressions Eqs. (22, 23,24) and putting the results into the Lagrange equation Eq. (20), the equations of motion are obtained as [18]

$$\mathbf{M}_{struct}\ddot{\mathbf{q}} + \mathbf{K}_{struct}\mathbf{q} = \mathbf{D}_{aero}\dot{\mathbf{q}} + \mathbf{K}_{aero}\mathbf{q} \tag{29}$$

This can, as in [18], be written as a generalised eigenvalue problem

$$\begin{bmatrix} \mathbf{0} & \mathbf{I} \\ (\mathbf{K}_{aero} - \mathbf{K}_{struct}) & \mathbf{D}_{aero} \end{bmatrix} \begin{bmatrix} \hat{\mathbf{q}} \\ \lambda\hat{\mathbf{q}} \end{bmatrix} = \begin{bmatrix} \mathbf{I} & \mathbf{0} \\ \mathbf{0} & \mathbf{M}_{struct} \end{bmatrix} \lambda \begin{bmatrix} \hat{\mathbf{q}} \\ \lambda\hat{\mathbf{q}} \end{bmatrix} \tag{30}$$

where $\mathbf{M}_{struct}$ and $\mathbf{K}_{struct}$ are the structural mass and stiffness matrices, respectively, and $\mathbf{D}_{aero}$ and $\mathbf{K}_{aero}$ denote the aerodynamic damping and "stiffness". The eigenvalues are given as $\lambda = -\zeta\omega \pm \imath\omega\sqrt{1-\zeta^2}$ [18]. The system becomes unstable when the damping ζ becomes negative $\mathfrak{Re}(\lambda) > 0$. In the stability limit $\zeta = 0$, the expressions for the eigenvalues simplify to $\lambda = \imath\omega$, so the frequency can be determined. The freestream velocity at this point is the critical flutter velocity. It is determined by increasing the velocity and solving the eigenvalue problem until the instability condition $\zeta = 0$ is encountered.

4 UNCERTAINTY QUANTIFICATION METHOD

While being the most simple and for its simplicity the most popular uncertainty quantification method, Monte Carlo methods suffer from the high number of calls to deterministic solvers, rendering their computational cost prohibitive. Polynomial chaos methods try to solve that problem by replacing the solver by a polynomial spectral decomposition of the stochastic response which acts as a surrogate model [24]

$$u(\boldsymbol{\theta}) \approx \sum_{i=1}^{\infty} \hat{u}_i \phi_i(\boldsymbol{\theta}) \tag{31}$$

where u is the stochastic response, which will be the critical flutter velocity V_f in this case, $\boldsymbol{\theta}$ is its stochastic input vector consisting of the uncertain polar parameters in this study, the ϕ_i are the orthogonal base polynomials and $\hat{u}_i$ are expansion coefficients weighting the base functions to obtain the correct response. Practically, the decomposition is cut off at a finite number of terms M, which depends on the number of stochastic parameters N and the polynomial order P [25]

$$M = \frac{(P+N)!}{P!N!} - 1 \tag{32}$$

As this number of terms increases rapidly with the number of stochastic parameters, constructing a model with the ply parameters as direct input would be too costly. Instead, we use the polar parameters, which reduces the number of stochastic inputs to six and makes the method thus applicable.

Initial development of the polynomial chaos method was for Gaussian distributions using Hermite polynomials [26]. The method was then generalised to a number of families of distributions using the polynomials in the Askey scheme [9]. Soize and Ghanem [13] provided the formalism to extend the method to arbitrary distributions by using orthogonalisation schemes to create the base functions. However, examples of applications on correlated variables were rare. This work will be based on a recent example by [14] which employs the Gram-Schmidt algorithm for the creation of said orthogonal polynomial basis.

In the framework of their method, orthogonality is defined with the help of a scalar product of functions as follows

$$\langle \phi_i, \phi_j \rangle = \int_{\boldsymbol{\Theta}} \phi_i(\boldsymbol{\theta}) \phi_j(\boldsymbol{\theta}) p(\boldsymbol{\theta}) d\boldsymbol{\theta} = \mathbb{E}\{\phi_i(\boldsymbol{\theta})^2\} \delta_{ij} \tag{33}$$

The Gram-Schmidt algorithm uses this scalar product to calculate coefficients c_{jk} that balance the total polynomial term in order to ensure that for each new term, the scalar product is zero. The procedure is then [14]

$$\phi_0(\boldsymbol{\theta}) = 1 \tag{34}$$

$$\phi_j(\boldsymbol{\theta}) = e_j(\boldsymbol{\theta}) - \sum_{k=0}^{j-1} c_{jk} \phi_k(\boldsymbol{\theta}) \tag{35}$$

where $e_j = \{1, \theta_1, \theta_2, \ldots, \theta_6, \theta_1^2, \theta_1\theta_2, \theta_1\theta_3, \ldots\}$.

The corresponding coefficients are

$$c_{jk} = \frac{\langle e_j(\boldsymbol{\theta}), \phi_k(\boldsymbol{\theta}) \rangle}{\langle \phi_k(\boldsymbol{\theta}), \phi_k(\boldsymbol{\theta}) \rangle} \tag{36}$$

where $\langle \cdot, \cdot \rangle$ is the scalar product defined in Eq. 33. When analytical expressions for the distribution or its characteristic or moment-generating functions are available, the polynomials can be

directly computed [14]. However, for the polar parameters, such expressions are not available to date. For this reason, Monte-Carlo integration is used to calculate the necessary integrals. As this only involves evaluation of polynomials, the computational cost of this operation remains low.

In ordinary polynomial chaos, the expansion coefficients from Eq. 31 are computed either through insertion of the chaos expansion into the Galerkin formulation [14] or in a way similar to the calculation of the orthogonalisation coefficients in the Gram-Schmidt process as [25]

$$\hat{u}_i = \frac{\langle u(\boldsymbol{\theta}), \phi_i(\boldsymbol{\theta}) \rangle}{\langle \phi_i(\boldsymbol{\theta}), \phi_i(\boldsymbol{\theta}) \rangle} \tag{37}$$

However, as the variable of interest, the critical flutter velocity V_f depends on a nonlinear instability root, the Galerkin formalism is not available in this case and the quadratures involved in the expression given above would require knowledge of the analytical expression for the distribution function. As this is not available, we resort to fitting to a random set of points in the parameter space via least-squares regression [6].

A graphical description of the full procedure to calculate the response surface using the arbitrary polynomial chaos (aPC) is given in Fig. 3.

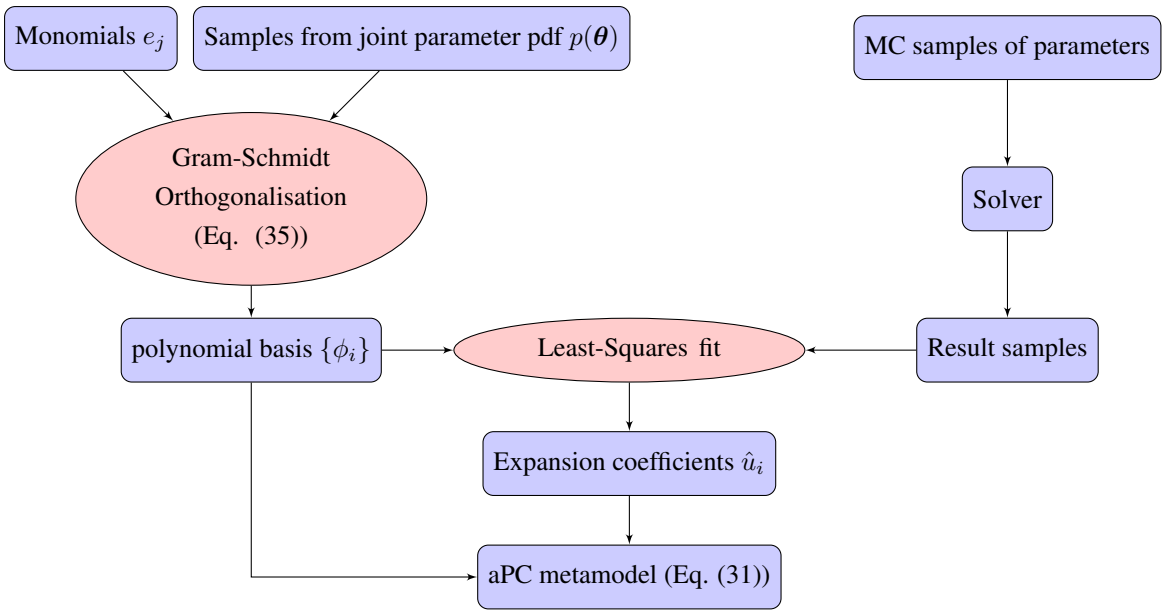

Figure 3: Scheme showing the steps of the aPC procedure

However, the response in critical flutter velocity to the material parameters is generally non-smooth, in which case global application of polynomial chaos methods fails [6]. Ibid., it was proposed to partition the parameter space and to apply the polynomial chaos to the different partitions. We present in the following a refined, fully automated method based on machine learning algorithms for this separation, in order to be able to use the arbitrary polynomial chaos methods in presence of the discontinuities in the response surface.

A key challenge in this problem is to identify the different modal regimes present in the aeroelastic response responsible for the discontinuities in critical flutter velocity. The present approach relies on a preliminary low-resolution Monte Carlo simulation, which results in example points

of the critical flutter velocity V_f and the flutter frequency ω_f, which is a strong indicator for a change in modal behaviour. An example data set issued from such a preliminary sampling is given in Fig. 4.

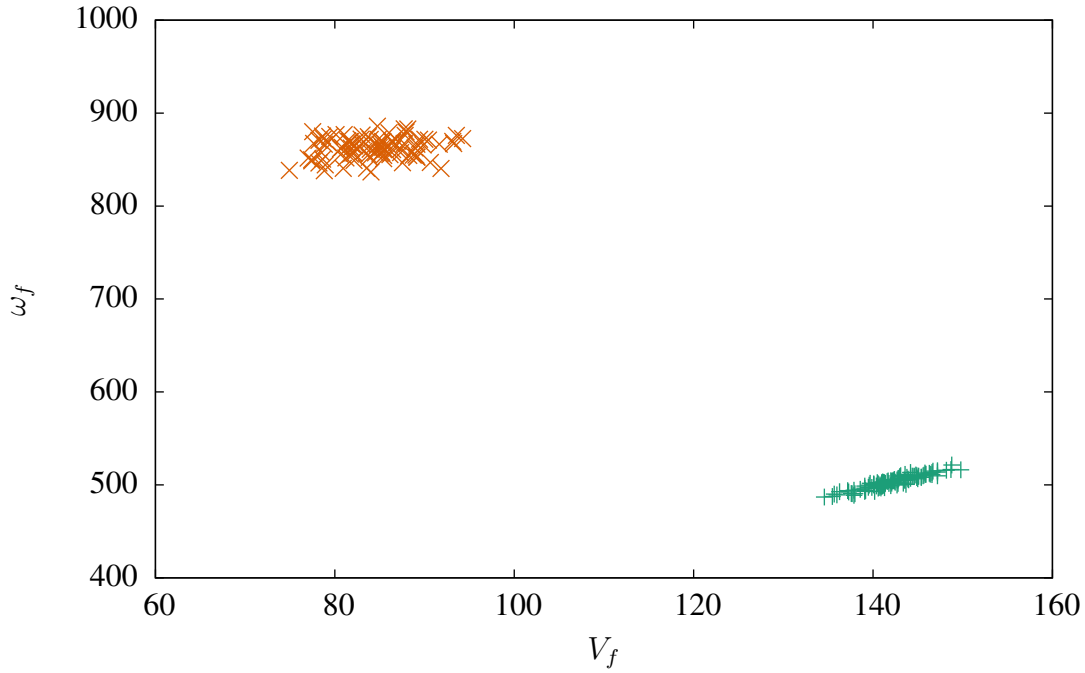

Figure 4: Clouds of example points showing V_f plotted against ω_f for configuration L1 (Table 7). The colors indicate the results of the DBSCAN clustering [27]

In most cases, the points are clearly different in either critical flutter velocity or flutter frequency, which leads to several regions with high densities of points separated by large areas with extremely low or zero point density. Using this convenient property, clustering is performed using the DBSCAN algorithm [27], which was designed exactly for that scenario. We use the implementation in *scikit-learn* [28], where we adjust the critical distance ϵ and the minimum number of samples to form a new cluster to prevent the algorithm from performing too many splits.

The labels gained from the clustering are then used to train a classification algorithm on the samples of material parameters associated to the V_f and ω_f samples used in the clustering, after a rescaling to operate on the real parts of the complex material constants Eq. (3) - (4) and scaling the data to zero mean and unit variance. The trained classifier is able afterwards to approximately tell the modal regime a sample will fall into, given only the values of the polar parameters. Different classification algorithms from *scikit-learn* were tested with their respective default parameters. The results are given in Table 3. As it performed best in the test, the Multi Layer Perceptron (MLP) classifier is chosen.

Algorithm	Correctly identified samples (%)
k Nearest Neighbours	92.9%
Support Vector Machine	96.1%
Multi Layer Perceptron Classifier	98.4%

Table 3: Percentage of correctly identified samples in a set of 100000 Monte Carlo samples for configuration L1 (see Table 7).

The trained classifier is then used to filter the samples for the construction of the polynomials and to attribute them to the different response surfaces. For the fitting, the clustered samples from the previous step are reused in order to avoid additional calls to the solver. The final sampling of the response surface is filtered by the classifier in the same way.

Fig. 5 provides a summary of the intervention points into the arbitrary polynomial chaos procedure given in Fig. 3.

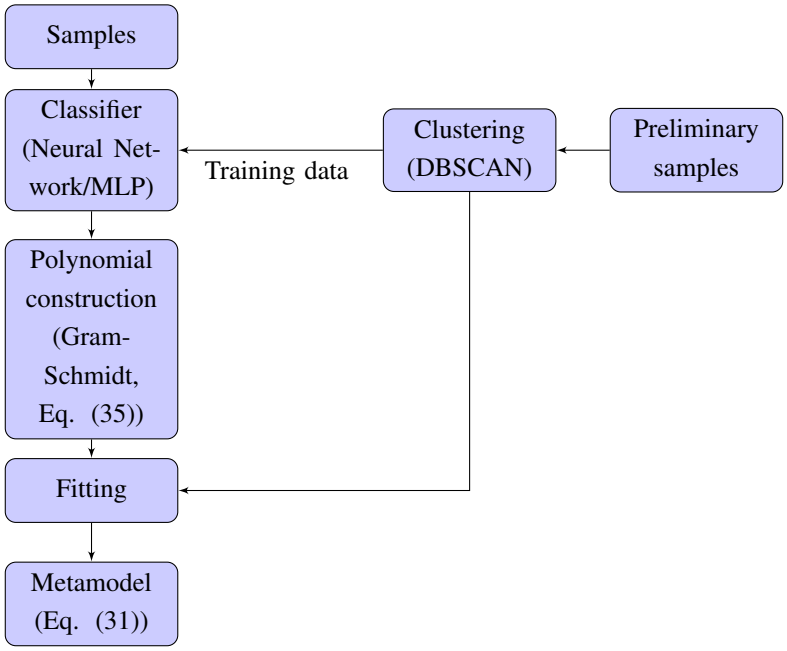

Figure 5: Intervention points of the machine learning approach employed in the aPC framework

5 RESULTS

In order to study the behaviour of wings as described in Section 2, we choose AS4/3502 as base material, which has been used before in studies on free vibration [1, 29] and aeroelasticity [2]. Its engineering moduli are given along with Poisson's ratio, the density and the ply thickness in Table 4.

$E_1[GPa]$	$E_2[GPa]$	$G_{12}[GPa]$	$\nu_{12}[-]$	$\rho[kg/m^3]$	Ply thickness $t[mm]$
138.0	8.96	7.1	0.3	1600	0.1

Table 4: Nominal orthotropic engineering modules of AS4/3502 UD tape

The corresponding polar parameters of the base layer are given in Table 5. The high values of the anisotropic polar parameters indicate a high degree of orientation of the elastic properties.

$T_0[GPa]$	$T_1[GPa]$	$R_0[GPa]$	$R_1[GPa]$	$\Phi_0[deg.]$	$\Phi_1[deg.]$
21.35	19.15	14.25	16.23	0	0

Table 5: Polar constants for the stiffness tensor of AS4/3502 UD tape

Starting from this base material, the domain of orthotropic layups with a thickness equivalent to a sixteen-ply layup will be studied. We will put the focus on a switch in modal behaviour in the said domain. Based on this preliminary deterministic study, specific layup configurations of which the nominal properties are close to the mode switch will be chosen, which will then be subject of a study of their behaviour in case of stochastic ply thickness and ply angle error.

5.1 Mode switching

Fig. 6 shows the aeroelastic response on the domain of the orthotropic laminates that can be created with the base material of which the elastic properties were given in Table 4 and Table 5, as defined by bounds Eqs. (11) - (14) and described in Fig. 1.

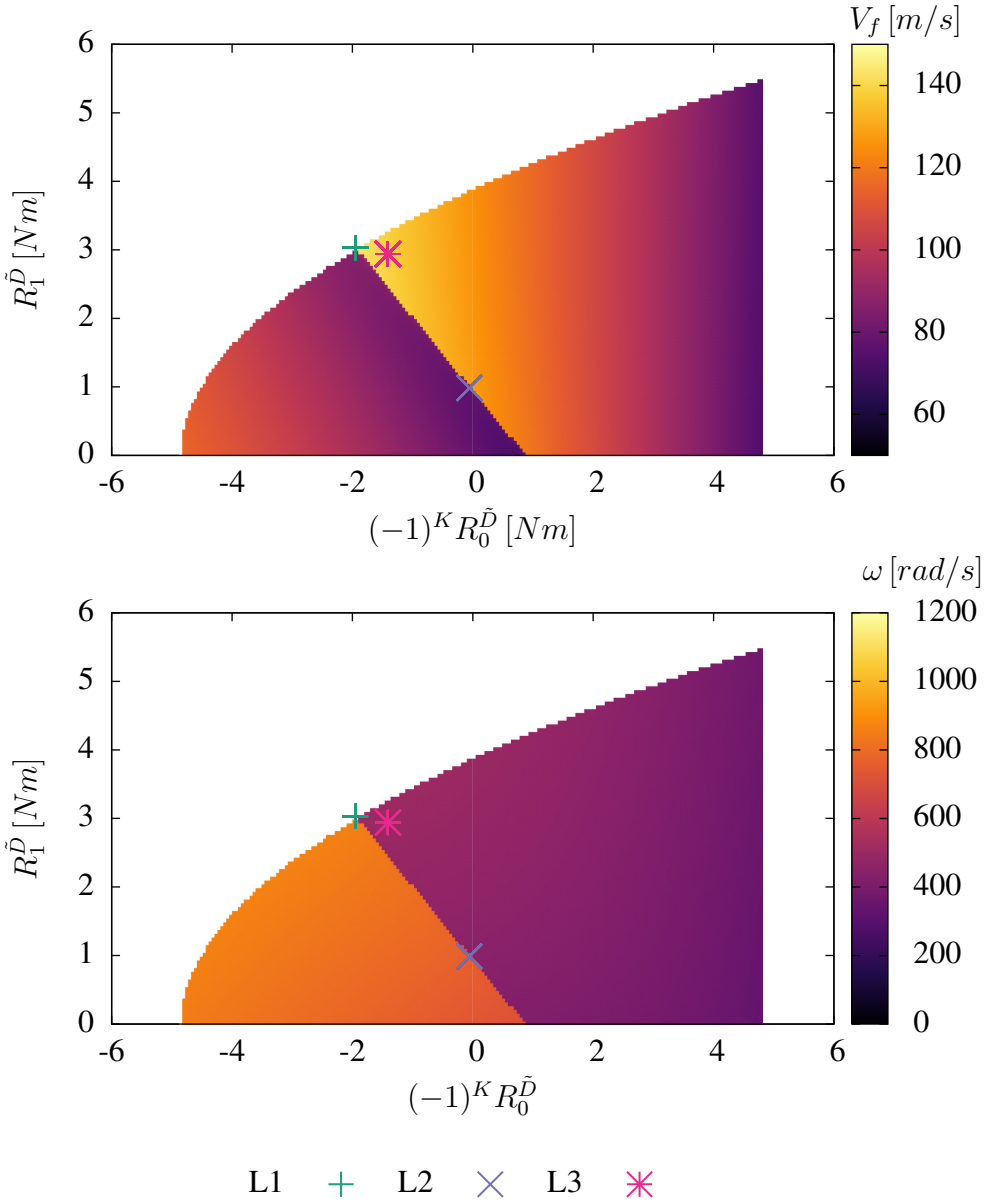

Figure 6: Response surface in critical flutter velocity and frequency. The examined configurations are marked with dots.

From left to the right, the critical flutter velocity declines, before increasing in a sudden step, which in this case spans over a straight line which can be described by the equation in the R_0-R_1

plane

$$\begin{bmatrix} (-1)^K R_0^{D,switch} \\ R_1^{D,switch} \end{bmatrix} = \begin{bmatrix} 0.92 \\ 0 \end{bmatrix} + t \begin{bmatrix} -2.87 \\ 3.03 \end{bmatrix}, t \in [0,1] \tag{38}$$

On the right of the step, the critical velocity decreases again. The step is also present in the frequency response, which otherwise presents less variation.

As the frequency response indicates, the step in the aeroelastic response is due to a switch in modal behaviour. Interestingly, the point corresponding to the maximal (optimal) critical flutter velocity lies on the upper border of the domain (see Fig. 6) and also on the border of the discontinuity. The corresponding stacking sequence is given in Table 7 as L1, which is an angle-ply laminate with ply angle 28.4 degrees.

The mode switch is demonstrated in Fig. 7 and Fig. 8. by showing two angle-ply laminate configurations which are offset by two degrees in ply angle from the aforementioned optimal configuration present on the upper left end of the mode switch. Both offset configrations lie on the upper border of the domain, but they are not depicted on Fig. 6, being very close point L1.

The first configuration is on the right of the mode switch and has the higher critical flutter velocity. Fig. 7b shows that the associated mode is a "first bending-dominated" mode, of which the real part of the corresponding eigenvalue is represented in Fig. 7a by the green line. It is clear from the eigenvalue plot that the mode is the first unstable mode since it is the first to cross the zero line, the event defining the critical flutter velocity.

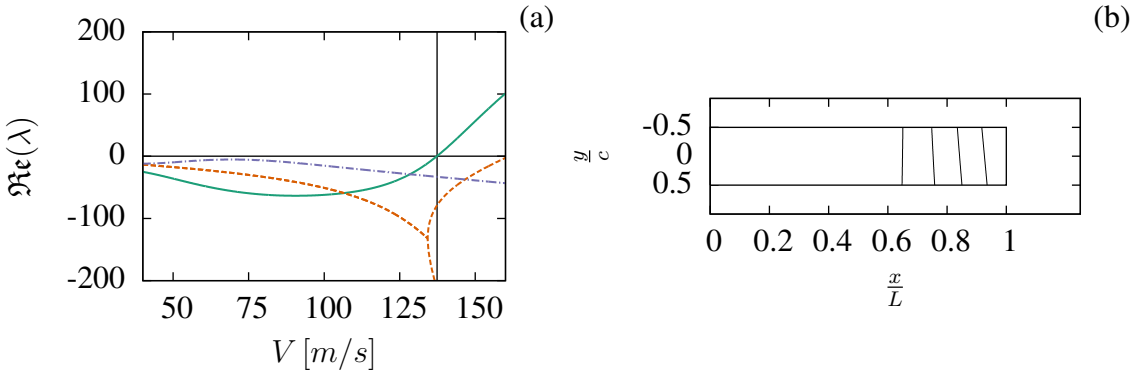

Figure 7: Stability plot and flutter mode for laminate with an offset of minus two degrees to the mode switch

As the material changes, the mode shapes change accordingly, which leads to the mode associated to the eigenvalue represented by the violet line becoming unstable (Fig. 8a). As its unstable region starts at lower velocities, the mode is the one defining the critical flutter velocity. The associated mode shape is a "second bending-dominated" mode.

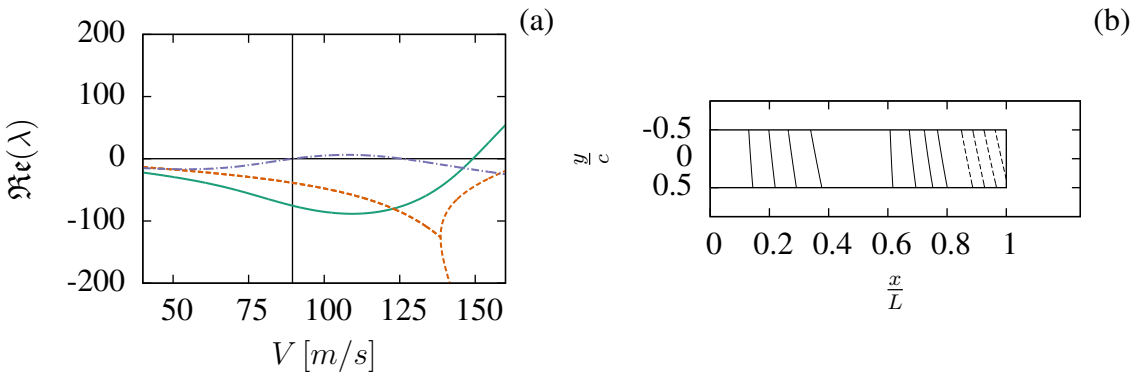

Figure 8: Stability plot and flutter mode for laminate with an offset of plus two degrees to the mode switch

We suspect that the mode switch in this case is triggered because the laminates get less and less stiff against bending from right to left, whereas the torsion stiffness increases. This might explain why more violent or higher order bending modes become more attractive to the left of the graph.

For a stochastic examination, three configurations are chosen from the polar domain along the mode switch. Their polar parameters are shown in Table 6 and their stacking sequences in Table 7.

- Layup L1 is the angle-ply laminate corresponding to the optimal (maximum) critical flutter velocity. It sits on the upper border of the polar domain Fig. 6, as well as on the upper point of the mode switch line. This laminate is uncoupled, homogeneous and orthotropic, with its principal axis of orthotropy aligned to the wing span.
- Layup L2 is a laminate that is much closer to the isotropic point (origin of the axis in Fig. 6). Orientation effects are consequently expected to be weaker. Nevertheless, it is also placed directly at the border to the mode switch. It is particular because one of its material invariants (R_0) almost vanishes, which might change its stochastic behaviour.
- Case L3 is chosen not to be directly next to the mode switch, but to have a small offset. It serves as a benchmark case to observe what happens if a laminate is only peripherably affected by the mode switch, and also to test the uncertainty quantification methodology.

Case	$T_0^{\tilde{D}}[Nm]$	$T_1^{\tilde{D}}[Nm]$	$(-1)^K R_0^{\tilde{D}}[Nm]$	$R_1^{\tilde{D}}[Nm]$	K	$\Phi_1^{\tilde{D}}[deg.]$	$V_f\,[m/s]$	$\omega_f\,[\frac{rad}{s}]$
L1	7.288	6.538	-1.948	3.032	1	0	143.48	505.24
L2	7.288	6.538	-0.056	0.986	1	0	127.96	450.24
L3	7.288	6.538	-1.408	2.941	1	0	138.67	499.83

Table 6: Polar properties of the different layups presented in Tab. 7

Case	Stacking sequence	Remarks
L1	$[28.4_2, -28.4_4, 28.4_2, -28.4_2, 28.4_4, -28.4_2]$	$V_{f_{max}}$
L2	$[\mp 27.6, 90, 27.6, 90, -27.6_2, \pm 27.6, 27.6_2, 90, -27.6, 90, \mp 27.6]$	—
L3	$[34, 0, -34_2, \pm 34, 34, 0_2, -34, \pm 34, 34_2, 0, -34]$	—

Table 7: List of laminates based on AS4/3502

5.2 Uncertainty propagation

In this work, we consider two main types of uncertainty inherent to the nature of the composite plate. One of them is the uncertainty in the ply thicknesses, which we consider distributed Gaussian with a coefficient of variation of about five percent. The second kind of uncertainty is the ply angles, which we also consider Gaussian with a standard deviation of one degree. A summary of the uncertainties is given in Table 8.

$\sigma_t[mm]$	0.005	$\sigma_\theta[deg.]$	1.0

Table 8: Standard deviations of the uncertainties in ply thicknesses and ply angles

These uncertainties are then propagated for each of the laminates listed in Table 7 through the arbitrary polynomial chaos procedure described in Fig. 3, with the machine learning procedures handling mode switches, if they occur, and splitting the response surfaces accordingly (Fig. 5). We use 10^3 samples of V_f and ω_f obtained by propagation through the aeroelastic solver for the preliminary sampling, where we did a convergence study to make sure the number of samples N_{mc} provides a certain robustness of the results. We use a feedback loop to ensure that each mode is sampled with a minimum number of preliminary samples of 10^2. Through this measure, the quality of the least-square fits of partial response surfaces is ensured. 10^5 Monte Carlo samples of the polar parameters are then used to calculate the orthogonal polynomial bases for the different response surfaces. This process does not involve calls to the aeroelastic solver. The polynomials are then fitted to the the preliminary samples of V_f. The final, assembled polynomial chaos model is then sampled using 10^5 samples of the polar parameters. This process does not involve calls to the aeroelastic solver, either. In summary, using the presented method, the number of calls to the aeroelastic solver decreases by a factor of up to 100 with respect to standard Monte Carlo simulation.

Fig. 9 shows the resulting distribution of the critical flutter velocity for layup L1 (Table 7). The distribution is multi-modal, which means that a mode switch has occured. The first mode is well distributed at values close to the nominal deterministic V_f value of about $143\,[m/s]$, (continuous vertical line in Fig. 9) although it shifts slightly to the left. The left-shift might come from the fact that the response surface is decreasing in one direction.

The second mode that takes values at much lower critical velocities of roughly between 70 and $100\,[m/s]$, which represents a major decrease from the nominal values. This second mode has a wider spread than the principal one, which is because the corresponding part of the response surface has higher gradients.

Along with the distribution and the nominal V_f value, we show a value at 15% below the nominal value which corresponds to a common flutter dimensioning criterion [30]. In this case, this corresponds to a value of about $122\,[m/s]$. We also present an estimate of the 1% quantile ($75\,[m/s]$). While the margin obviously misses the start of flutter for the stochastic configurations, the 1% quantile estimate provides a more robust indicator.

The comparison with a Monte Carlo simulation shows that the arbitrary polynomial chaos model succeeds in representing the stochastic response surface with satisfactory accuracy.

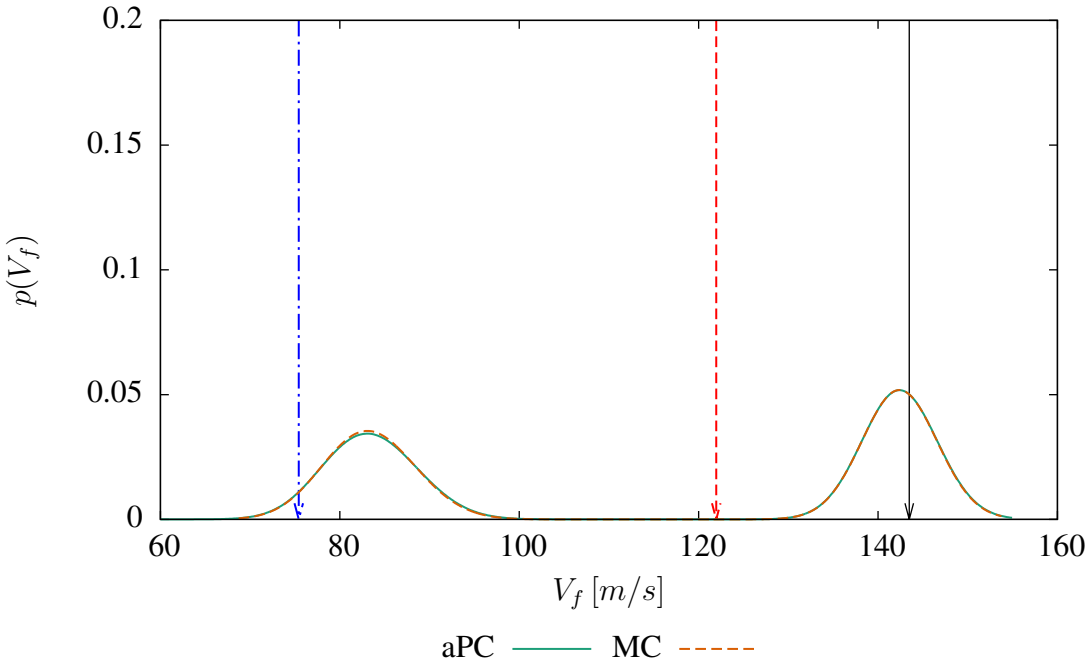

Figure 9: Distribution of critical flutter velocity V_f for layup L1. The black vertical bar is the nominal value, the red bar a 15% margin based on the nominal value and the blue line is an estimation of the 1% quantile for the critical flutter velocity.

The stochastic flutter results for layup L2 (Table 7) are shown in Fig. 10. Again, the distribution is bimodal, which means that a mode switch has been triggered. Despite the fact that the nominal laminate configuration is placed very far from the previous example in the polar orthotropic domain, it behaves in a very similar manner. The slight offset of the probability maximum in the probability density function mode observed in Fig. 9 is also observed in this example, as well as the inferior probability density function mode spreading wider than the one closer to the nominal V_f value. However, compared to the previous example, the individual modes show a smaller variance. This could be due to the different response in this region, but also be due to a layup more robust to stochastic perturbations.

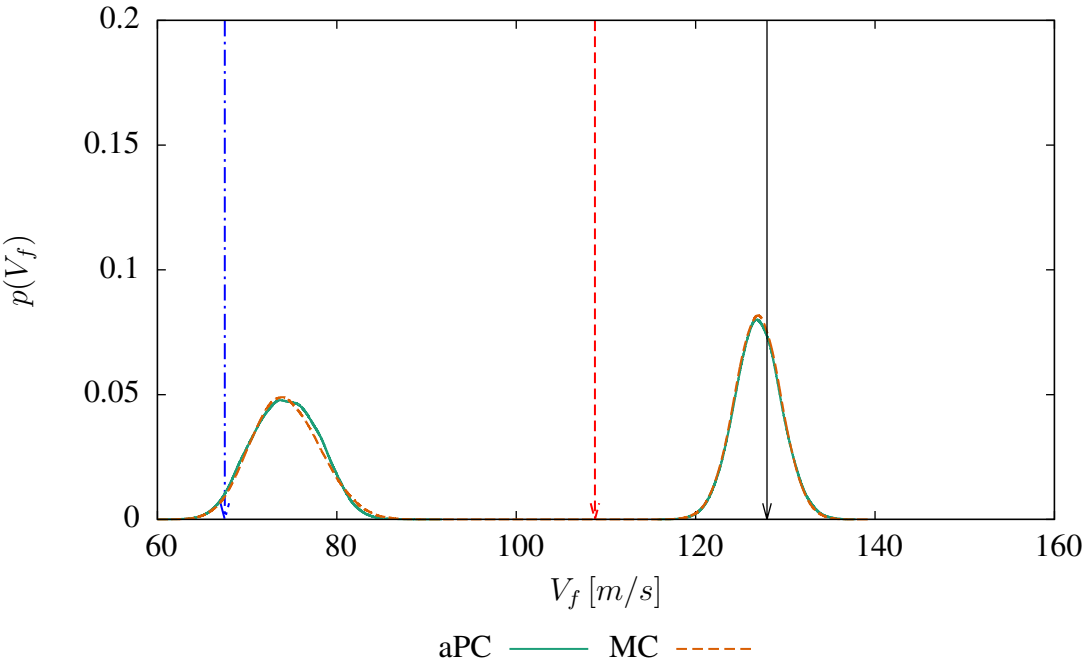

Figure 10: Distribution of critical flutter velocity V_f for layup L2. The black vertical bar is the nominal value, the red bar a 15% margin based on the nominal value and the blue line is an estimation of the 1% quantile for the critical flutter velocity.

The last case of laminate L3 serves as a benchmark for the uncertainty quantification method, particularly the separation of the response surfaces by the machine learning procedure. It is not placed in direct vicinity to the mode switch, but is offset by about 1.5 standard deviations from the configuration that flutters. The results are shown in Fig. 11.

In this case, the low-velocity probability density function mode represents a much smaller probability mass than the principal probability density function mode located close to the nominal value. The latter is also distributed much more symmetrically around the nominal value than in the previous examples.

While this principal probability density function mode is well resolved by the uncertainty quantification method, the method struggles more with the lower velocity mode, which can be seen in the comparison to the plain Monte Carlo simulation. Its spread is also estimated too wide. However, it can still provide information about the mode switch occuring, which is also indicated by the quantile estimate based on it.

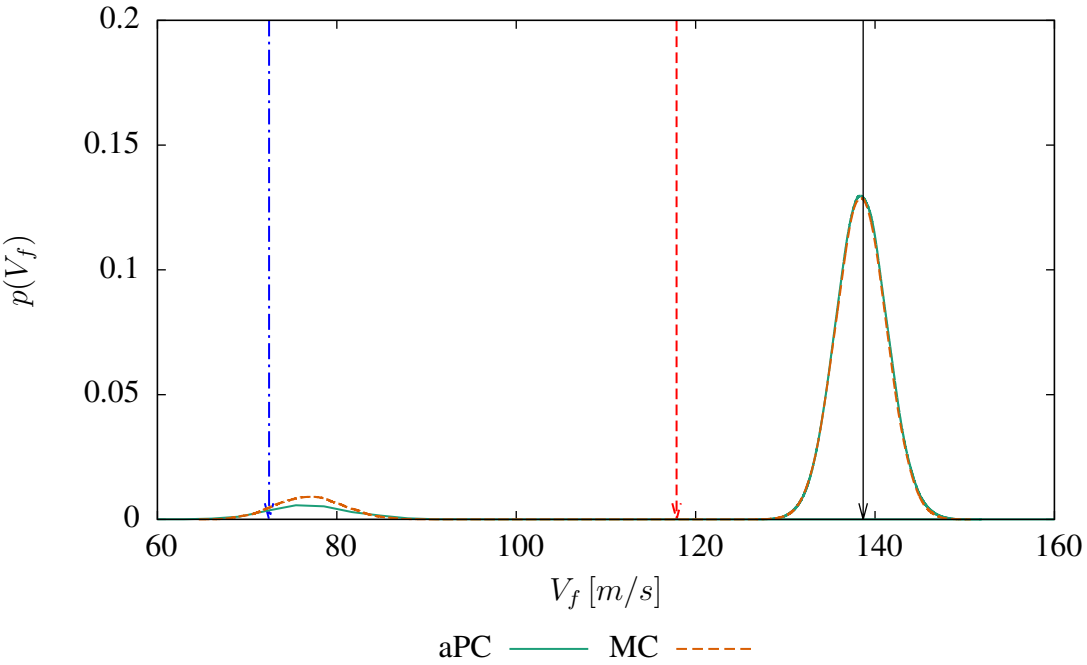

Figure 11: Distribution of critical flutter velocity V_f for layup L3. The black vertical bar is the nominal value, the red bar a 15% margin based on the nominal value and the blue line is an estimation of the 1% quantile for the critical flutter velocity.

6 CONCLUSION

In this work, stochastic flutter prediction taking into account the inherent uncertainty in the composite material was carried out by coupling the polar method with aPC dedicated to correlated random variables. Results show changes in the modal behaviour with respect to the uncertain parameters. The important changes in the critical flutter velocity due to the mode change are well handled by the response surface splitting procedure based on machine-learning, permitting quite accurate predictions of the critical flutter velocity across the mode switch.

The present investigation makes clear that uncertainty quantification is a valuable tool for flutter risk evaluation. It has been shown to provide additional security over the classical flutter margin in case of mode switches which often change the critical flutter velocity by far more than the canonical 15%, the security margin given assumed in classical flutter analysis.

While this investigation represents a working proof-of-concept and was able to highlight the benefits of stochastic methodology, it has to become more precise to be useful for robust optimisation and risk-analysis-based design. To achieve this, more advanced approximations of the distributions of the polar parameters have to be developed, along with a resolution of the polynomial chaos approximation by quadrature. This would enable error estimates on the quantiles, which in turn enables adaptivity and taking into account rare events.

REFERENCES

[1] Jensen, D., Crawley, E., and Dugundji, J. (1982). Vibration of Cantilevered Graphite/Epoxy Plates With Bending-Torsion Coupling. *Journal of Reinforced Plastics and Composites*, 1(3), 254–269. ISSN 0731-6844.

[2] Hollowell, S. J. and Dugundji, J. (1984). Aeroelastic flutter and divergence of stiffness coupled, graphite/epoxy cantilevered plates. *Journal of Aircraft*, 21(1), 69–76. ISSN 0021-8669, 1533-3868.

[3] Sriramula, S. and Chryssanthopoulos, M. K. (2009). Quantification of uncertainty modelling in stochastic analysis of FRP composites. *Composites Part A: Applied Science and Manufacturing*, 40(11), 1673–1684. ISSN 1359835X.

[4] Uhart, M., Patrouix, O., and Aoustin, Y. (2014). Improving accuracy in robotized fibre placement using force and visual servoing external hybrid control scheme.

[5] Wang, Q. (2008). *Uncertainty quantification for unsteady fluid flow using adjoint-based approaches*. Ph.D. thesis, Stanford University.

[6] Scarth, C., Cooper, J. E., Weaver, P. M., et al. (2014). Uncertainty quantification of aeroelastic stability of composite plate wings using lamination parameters. *Composite Structures*, 116, 84–93. ISSN 02638223.

[7] Verchery, G. (1979). Les invariants des tenseurs d'ordre 4 du type de l'élasticité. In *Comportment Méchanique des Solides Anisotropes*, vol. 115. Villard-de-Lans: Éditions du CNRS, Paris, pp. 93–104.

[8] Vannucci, P. (2005). Plane Anisotropy by the Polar Method*. *Meccanica*, 40(4-6), 437–454. ISSN 0025-6455, 1572-9648.

[9] Xiu, D. and Karniadakis, G. E. (2002). The Wiener–Askey Polynomial Chaos for Stochastic Differential Equations. *SIAM Journal on Scientific Computing*, 24(2), 619–644. ISSN 1064-8275, 1095-7197.

[10] Xiu, D., Lucor, D., Su, C.-H., et al. (2002). Stochastic Modeling of Flow-Structure Interactions Using Generalized Polynomial Chaos. *Journal of Fluids Engineering*, 124(1), 51. ISSN 00982202.

[11] Lucor, D., Xiu, D., Su, C.-H., et al. (2003). Predictability and uncertainty in cfd. *International Journal for Numerical Methods in Fluids*, 43(5), 483–505. ISSN 1097-0363.

[12] Le Meitour, J., Lucor, D., and Chassaing, J.-C. (2010). Prediction of stochastic limit cycle oscillations using an adaptive Polynomial Chaos method. *Journal of Aeroelasticity and Structural Dynamics*, 2(1), 1–20. ISSN 1974-5117. doi:10.3293/asdj.2010.4.

[13] Soize, C. and Ghanem, R. (2004). Physical Systems with Random Uncertainties: Chaos Representations with Arbitrary Probability Measure. *SIAM Journal on Scientific Computing*, 26(2), 395–410. ISSN 1064-8275, 1095-7197.

[14] Navarro Jimenez, M.I., Witteveen, J.A.S., and Blom, J.G. (2014). Polynomial Chaos Expansion for general multivariate distributions with correlated variables. Tech. rep., Centrum Wiskunde & Informatica.

[15] Nitschke, C., Maruani, J., Vincenti, A., et al. (2015). UNCERTAINTY QUANTIFICATION IN AEROELASTIC RESPONSE OF AN IDEALIZED COMPOSITE WING. In *International Forum on Aeroelasticity and Structural Dynamics*, vol. 2. St Petersburg, Russia, pp. 970–983.

[16] Vannucci, P. (2002). A Special Planar Orthotropic Material. *Journal of elasticity and the physical science of solids*, 67(2), 81–96. ISSN 1573-2681.

[17] Vannucci, P. (2013). A Note on the Elastic and Geometric Bounds for Composite Laminates. *Journal of Elasticity*, 112(2), 199–215. ISSN 0374-3535, 1573-2681.

[18] Wright, J. R. and Cooper, J. E. (2015). *Introduction to aircraft aeroelasticity and loads*. Chichester: Wiley, 2. ed ed. ISBN 978-1-118-48801-0 978-1-118-48801-0 978-1-118-70042-6.

[19] Stodieck, O., Cooper, J. E., Weaver, P. M., et al. (2013). Improved aeroelastic tailoring using tow-steered composites. *Composite Structures*, 106, 703–715. ISSN 02638223.

[20] Stein, W. (2010). A summary of Classical Lamination Theory. Retrieved on February 25th, 2015.

[21] Minich, M. D. and Chamis, C. C. (1975). Analytical displacements and vibrations of cantilevered unsymmetric fiber composite laminates. In *AIAA, ASME, and SAE, Structures, Structural Dynamics, and Materials Conference*. Denver, Colorado.

[22] Leissa, A. W. (1973). The free vibration of rectangular plates. *Journal of Sound and Vibration*, 31(3), 257–293. ISSN 0022460X.

[23] Reddy, J. N. (1999). *Theory and analysis of elastic plates*. Philadelphia, PA: Taylor & Francis. ISBN 1-56032-705-7 978-1-56032-705-9.

[24] Lucor, D. (2012). Introduction to Uncertainty Quantification in Computational Fluid Dynamics. Lecture Notes of NSE22 2012, held at Université Pierre et Marie Curie Paris 6.

[25] Le Meitour, J., Lucor, D., and Chassaing, J.-C. (2010). Prediction of stochastic limit cycle oscillations using an adaptive Polynomial Chaos method. *Journal of Aeroelasticity and Structural Dynamics*, 2(1), 1–20. ISSN 1974-5117.

[26] Wiener, N. (1938). The Homogeneous Chaos. *American Journal of Mathematics*, 60(4), pp. 897–936. ISSN 00029327.

[27] Ester, M., Kriegel, H.-P., Sander, J., et al. (1996). A density-based algorithm for discovering clusters in large spatial databases with noise. In *Proceedings of the Second International Conference on Knowledge Discovery and Data Mining*, vol. 96. pp. 226–231.

[28] Pedregosa, F., Varoquaux, G., Gramfort, A., et al. (2011). Scikit-learn: Machine Learning in Python. *Journal of Machine Learning Research*, 12, 2825–2830.

[29] Qatu, M. S. (1991). Free vibration of laminated composite rectangular plates. *International Journal of Solids and Structures*, 28(8), 941–954. ISSN 00207683.

[30] Federal Aviation Administration (2014). Aeroelastic Stability Substantiation of Transport Category Airplanes. Advisory Circular 25.629-1B, U.S. Department of Transportation, Federal Aviation Administration, Washington, D.C.